Volume 7
Number 19
7 October 2023
Pages 4699–4996

Sustainable Energy & Fuels

Interdisciplinary research for the development of sustainable energy technologies

rsc.li/sustainable-energy

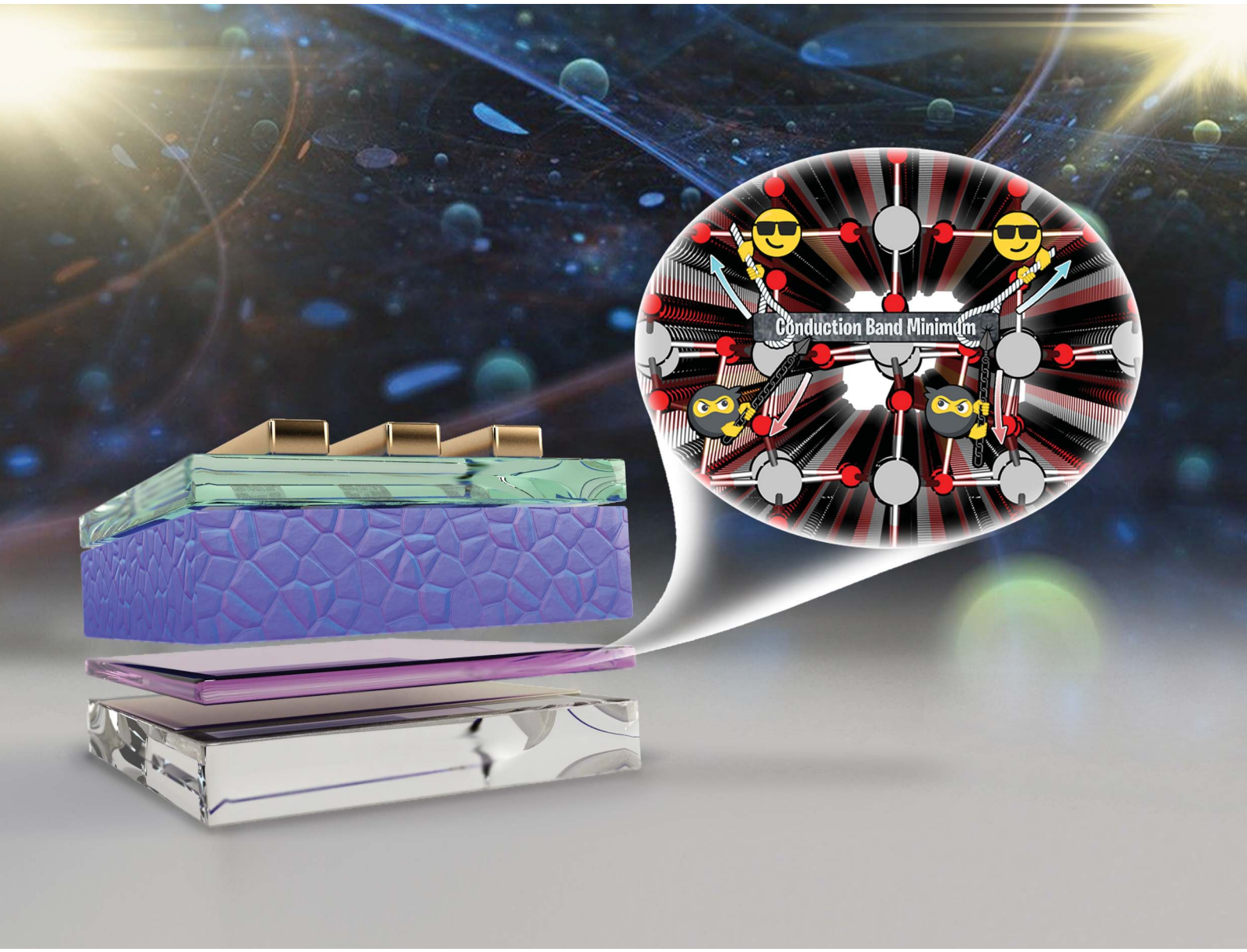

ISSN 2398-4902

ROYAL SOCIETY OF CHEMISTRY

PAPER

Michele Pavone, Ana Belén Muñoz-García *et al.*
The role of Mg dopant concentration in tuning the performance of the SnO_2 electron transport layer in perovskite solar cells

Sustainable Energy & Fuels

ROYAL SOCIETY OF CHEMISTRY

PAPER

View Article Online
View Journal | View Issue

Cite this: *Sustainable Energy Fuels*, 2023, 7, 4855

The role of Mg dopant concentration in tuning the performance of the SnO_2 electron transport layer in perovskite solar cells

Gennaro Vincenzo Sannino,[ab] Adriana Pecoraro,[bc] Pasqualino Maddalena,[c] Annalisa Bruno,[de] Paola Delli Veneri,[d] Michele Pavone *[ab] and Ana Belén Muñoz-García *[bc]

Recent experiments pointed out a beneficial role of moderate Mg doping in SnO_2 for application as an electron transport layer (ETL) in perovskite solar cells. The high efficiencies obtained with Mg-doped SnO_2 are driven by an improved open circuit potential (V_{OC}), but the origin of this behaviour is still under debate. Some ascribe this enhancement to the improved quality of the thin ETL film, while others speculate it is due to an electronic structure rearrangement upon Mg doping. In this context, here we applied density functional theory calculations to uncover the changes in SnO_2 structural, electronic, and defect properties induced by different percentages of Mg doping. Our predictions of conduction band minimum (CBM) variations provide new insights on the trend of different V_{OC} values observed in experiments. We found that low Mg contents push up the SnO_2 CBM increasing the V_{OC}. In contrast, at high dopant concentration, interstitial Mg defects are more likely to occur, leading to lower V_{OC} and to the formation of intra-gap band states, explaining the decrease of PSC performances at a high Mg doping ratio. These findings provide a new atomistic perspective on the positive/negative effects of Mg dopants for the application of SnO_2 in last-generation solar cells, highlighting key structural and defect properties that can be easily tuned to obtain ETL materials with purposely tailored electronic features.

Received 17th March 2023
Accepted 14th July 2023

DOI: 10.1039/d3se00362k

rsc.li/sustainable-energy

Introduction

Some metal oxides have the unique characteristic of being both electrically conductive and optically transparent in the visible region. Tin dioxide (SnO_2) for example has attracted much attention for its applications as a transparent conducting oxide in different fields, such as solar cells,[1,2] gas sensors,[3,4] display devices,[5] and lithium-ion batteries.[6] SnO_2 is intrinsically an n-type semiconductor due to the presence of native point defects[7,8] and its optical band gap ranges from 3.6 to over 4.0 eV,[9] ensuring a high optical transmittance (>80%) in the visible range.[10] Noteworthily, it is also highly stable both thermally and chemically, and abundant in nature.

The electronic and structural properties of SnO_2 have been purposely tuned for different applications *via* doping with several possible elements. Donor dopants are widely used[11,12] to increase the density of the majority carriers and produce an n-type SnO_2 transparent electrode. Other dopants, such as Zn and Ni, are used to promote gas sensing properties[13–15] and improve its performances as an electron transport layer (ETL) in perovskite solar cells (PSCs).[16–19] Induction of ferromagnetic properties, a key feature for spintronic applications, has also been predicted *via ab initio* calculations and obtained experimentally with transition metal and non-magnetic doping elements.[20–24] SnO_2 can be doped instead with acceptor atoms but whether p-type conduction can be achieved in SnO_2 using acceptor dopants is still an open question. Theoretical calculations considering different dopants (*e.g.*, Al, Ga, In interstitial or substituting Sn, N substituting O and Li substituting Sn) indicate that different kinds of trapping states preclude SnO_2 from having p-type character.[25] On the other hand, p-type SnO_2 films have already been fabricated, although with low conductivity. For example, In-doped SnO_2 films with p-type conduction have been prepared and characterized in different studies,[26–28] and Othmen *et al.*[29] have demonstrated the applicability of p-type highly Fe-doped SnO_2 thin films in homojunctions with non-doped SnO_2. Several studies have reported the effects generated by Mg-doping in SnO_2. Early studies by Li *et al.*[30] have analyzed the morphological and optical properties of Mg-doped SnO_2 thin films. He *et al.*[31,32] have calculated the defect energy

[a]*Department of Chemical Sciences, University of Naples Federico II, Napoli, Italy. E-mail: michele.pavone@unina.it*

[b]*INSTM-GISEL, National Interuniversity Consortium of Materials Science and Technology (INSTM), Florence, Italy. E-mail: anabelen.munozgarcia@unina.it*

[c]*Department of Physics "E. Pancini", University of Naples Federico II, Napoli, Italy*

[d]*Italian National Agency for New Technologies, Energy and Sustainable Economic Development, (ENEA), Portici, (Na), Italy*

[e]*Energy Research Institute @ NTU (ERI@N), Nanyang Technological University, Singapore*

formation and the hole concentration indicating that Mg is suitable for doping of SnO_2 and, recently, Fu and co-workers[33] have developed a fabrication method to generate Mg-doped SnO_2 film. Mg has also been reported to confer peculiar magnetic properties to SnO_2 such as room-temperature ferromagnetism.[23,34] Recent studies by Xiong *et al.*[35] and Zhou *et al.*[36] also pointed out the beneficial role of Mg doping in perovskite solar cell (PSC) performances. Indeed, doping with Mg^{2+} partially substituting Sn^{4+} ions has been reported to tune SnO_2 properties without compromising its n-type character. Fabricated devices have reached higher efficiencies when Mg-doped SnO_2 film has been used as the ETL compared to the pristine material. However, there is no consensus on the exact role of Mg in such improvement. Xiong *et al.* reported better quality of the Mg-doped film deposited *via* high-temperature treatment with respect to the undoped one and, consequently, suggest a better interfacial contact with the perovskite. In terms of performance, their PSCs are reported to attain the best power conversion efficiency (PCE) with a 7.5% Mg content, whilst higher doping percentages (10 and 20%) result in lower PCEs. Devices fabricated by Zhou have shown higher V_{OC}, and a lower charge extraction ability for Mg-doped SnO_2 films, which has been ascribed to a slight rise in SnO_2 conduction band minimum potential upon Mg doping. These findings do not match the UPS measurements performed by Xiong, which reveal a lower CBM for doped films, not correlated with doping concentration and V_{OC} values obtained from complete devices. This puzzling electronic behavior of Mg-doped SnO_2 motivates the present work, which aims at assessing the effects of different Mg doping concentrations on the electronic properties of SnO_2 as the ETL using atomistic simulations based on the density functional theory (DFT). In particular, we address the enhanced-to-thwarted performance switch of Mg-doped SnO_2 as the ETL in PSCs when going from low to moderate doping degrees.

Since the band alignment between the ETL CBM and the perovskite CB is crucial in this kind of devices, any energy shift of the valence and/or conduction bands related to work function (WF) changes can affect the working mechanism and the solar cell parameters. After presenting (Mg-doped) SnO_2 bulk properties, we exploit the surface-slab approach to calculate ΔCBM to explain, from an electronic point of view, the enhancement in performances and V_{OC} reported in the literature[35,36] for Mg-doped SnO_2-based PSCs. In our models Sn^{4+} ions are substituted with Mg^{2+} but, given the limited solubility,[23] we have considered both substitutional and interstitial Mg^{2+} ions at high doping concentrations. We want to emphasize that the wording "Mg-doped SnO_2" denotes, from now on, the addition of Mg^{2+} acceptor defects in SnO_2, preserving its n-type character.

Our study provides a fundamental understanding of the effective positive role of low dosage of Mg doping, which increases the CBM of the SnO_2 providing higher V_{OC} and enhances the PCE of PSCs and of the negative role of the high doping concentrations where Mg^{2+} occupy interstitial sites, which is detrimental for the PCE of the PSCs. Furthermore, our findings pave the way for a new structure-based approach for the design of doping for materials most used as ETLs.

Methods and computational details

Our first-principles spin-polarized DFT calculations have been performed within periodic boundary conditions and a plane wave/pseudopotential approach, as implemented in the Vienna *ab initio* simulation package (VASP, version 5.4.4) code.[37–40] For structural optimizations and electronic structure calculations we applied Perdew, Burke, and Ernzerhof (PBE) GGA exchange–correlation density functional,[41,42] as well as the Heyd–Scuseria–Ernzerhof (HSE06)[43,44] hybrid functional. All atomic positions have been allowed to relax without imposing symmetry constraints until residual forces on each atom were smaller than 0.03 eV $Å^{-1}$. All ionic cores have been represented by projector-augmented wave (PAW) potentials:[45,46] $2s^2 2p^4$ electrons for O, $5s^2 5p^2$ electrons for Sn, and $3s^2$ electrons for Mg were treated as valence electrons. Dispersion forces have been accounted for with Grimme's D3 (ref. 47) with the damping scheme by Becke and Johnson (D3BJ).[48] We use the BJ damping to deal with dispersion interactions at short distances and mitigate the double-counting of electron correlation effects at intermediate distances. We chose an SCF energy threshold of 10^{-5} eV and a plane wave energy cut-off at 600 eV in all calculations. Γ-centered Monkhorst–Pack *k*-point grids of $6 \times 6 \times 9$, $3 \times 3 \times 3$, $3 \times 5 \times 1$, and $2 \times 3 \times 1$ have been used for the SnO_2 bulk unit cell, (Mg-)SnO_2 bulk supercell, and (Mg-)SnO_2 slab models described below at PBE-D3BJ and HSE06-D3BJ levels of theory, respectively. These approaches have been widely exploited for several transition metal oxide bulk and surfaces.[49–53]

Geometry optimization has been performed starting from experimental lattice constants and atomic parameters[54] of the $P4_2/mnm$ space group. The pristine bulk structure has been optimized at both PBE-D3BJ and HSE06-D3BJ levels of theory. A 96-atom supercell (32 f.u.) has been considered as the starting point to simulate different Mg concentrations in Mg-doped SnO_2. Lattice constants of doped bulk supercells have been fixed to an integer multiple values of those PBE-D3BJ optimized for the undoped material since Mg^{2+} and Sn^{4+} ions in VI coordination have similar dimensions (~0.7 Å).[55] Subsequently, HSE06-D3BJ single point calculations have been performed on geometries optimized at the PBE-D3BJ level of theory.

Work functions have been computed from slab models of undoped and Mg-doped SnO_2 surfaces. Our models have been built with the (110) surface termination, identified as the most stable surface.[56,57] On the surface plane, our model consisted of a 3×1 supercell of the (110) unit cell. As for slab thickness, we employed five O–Sn–O tri-layers which ensured converged surface energy within 5×10^{-4} J m^{-2}. This supercell and thickness choice resulted in 90-atom slabs. We used a vacuum layer >10 Å to avoid any interaction between images. The work function of pristine (0% Mg) and doped SnO_2 has been calculated at the HSE06-D3BJ level of theory on PBE-D3BJ optimized geometries from the planar-average electrostatic potential (PAEP) of such slabs as follows:[58]

$$WF_{(x\%Mg)} = E_{vac} - E_{VB},\ x = 0,\ 3,\ 6,\ 10\%$$

Table 1 Calculated and experimental lattice constants of SnO_2 (relative errors in parenthesis) and eigenvalue gap values (E_g)

	PBE-D3BJ	HSE06-D3BJ	Exp.
$a = b$ (Å)	4.797 (+1.25%)	4.727 (−0.21%)	4.737 (ref. 54)
c (Å)	3.226 (+1.24%)	3.179 (−0.22%)	3.186 (ref. 54)
E_g (eV)	0.80	3.04	3.6 (ref. 60)

where E_{vac} is the value of the PAEP in the vacuum region of the slab model and E_{VB} is the energy of the highest occupied level. In the approximation of the rigid band model, the WF values provide information to extrapolate the changes in the CBM ($\Delta CBM = (CBM_{(x\%Mg)} - CBM_{(0\%Mg)})$) of the doped SnO_2 material. A lower WF points out higher CBM. Thus, the change in WF ($\Delta WF = (WF_{(x\%Mg)} - WF_{(0\%Mg)})$) is the opposite of ΔCBM. Finally, the trend in V_{OC} has been connected with the ΔCBM.

Results and discussion

SnO_2 pristine bulk structure has been analysed from the structural and electronic points of view with PBE-D3BJ and hybrid HSE06-D3BJ density functionals. Table 1 lists computed lattice parameters and eigenvalue gaps for both exchange–correlation functionals. As reported in other theoretical studies,[56,57,59] lattice parameters predicted by PBE were overestimated within the expected error (∼1.2%). HSE06 hybrid functional provided slightly underestimated lattice constant values in better agreement with the experiments with percentage errors of ∼0.2% along all three lattice vectors.

As expected, energy bandgap values extracted from these calculations are highly dependent on the used exchange–correlation functionals. The experimental band gap (3.6 eV)[60] is underestimated by PBE (0.80 eV), consistently with other DFT studies on SnO_2,[61–63] whilst HSE06 functionals predicted a wider eigenvalue gap 3.04 eV, closer to the experimental value.

Computed band structures and pDOS plots of undoped SnO_2 at PBE-D3BJ and HSE06-D3BJ levels of theory (depicted in Fig. 1) match what has been reported in previous studies.[64,65] Except for the bandgap value itself, both levels of theory predicted qualitative identical pDOS and band structures, featuring a direct band gap at the Γ point, Oxygen p states are the main contributors to the edge of the valence band, and Sn s states to the bottom part of the CB.

We adopted the supercell approach for Mg-doped SnO_2 bulk at different doping levels. 1, 2, or 3 Sn atoms were replaced with Mg in the 96-atom supercell (32 f.u.) to reproduce 3, 6, or 9% doping percentages, respectively. For 6% and 9% cases, substituted atoms have been placed as far as possible from each other (minimum distance ∼ 5 Å) (Fig. 2). As reported in previous studies,[66–68] replacement of Sn by Mg does not induce remarkable changes in optimized lattice parameters due to the very similar ionic radii of Sn^{4+} and Mg^{2+}, respectively 0.69 and 0.72 Å.[55] For this reason, we use the (scaled) lattice constants of pristine SnO_2 also for the doped systems. Fig. 2 shows the total DOS calculated at the HSE06-D3BJ level of theory on PBE-D3BJ optimized geometries for all the considered doping percentages. We do not report spin-projected DOS as the discussion of magnetic properties is outside the scope of our work. The valence band (VB) crossed the Fermi level in doped bulks, pointing out the p-type behavior of the doped material.

Starting from the 5L-(110) slab model containing 90 atoms (30 f.u.), 1, 2 or 3 inner Sn atoms were substituted with Mg to describe 3, 6, or 10% doping contents, respectively, as done for the bulk. Aiming at assessing the effect of substitutional *vs.* interstitial Mg doping, we have also considered two alternative 6% and 10% doped systems (labeled as 6%* and 10%*) where one and two Mg atoms, respectively, do not substitute Sn but fill interstitial lattice sites. In the 6%* and 10%* systems, a tin vacancy is associated with each interstitial Mg to keep the same stoichiometry as in 6% and 10%. For all these models, we have performed HSE06-D3BJ single point calculations on PBE-D3BJ optimized geometries, which are depicted in Fig. 3 together with the corresponding pDOS plots.

While the presence of Mg in the interstitial site is energetically unfavorable, the energy differences calculated between the "pure" substitutional slabs and the corresponding interstitial Mg counterparts are relatively small (0.15 and 0.21 eV f.u.$^{-1}$ for 6% and 10%, respectively) so we can consider that both configurations are likely to occur.

While systems with substitutional doping presented p-type pDOS similar to those of bulk materials, the pDOS

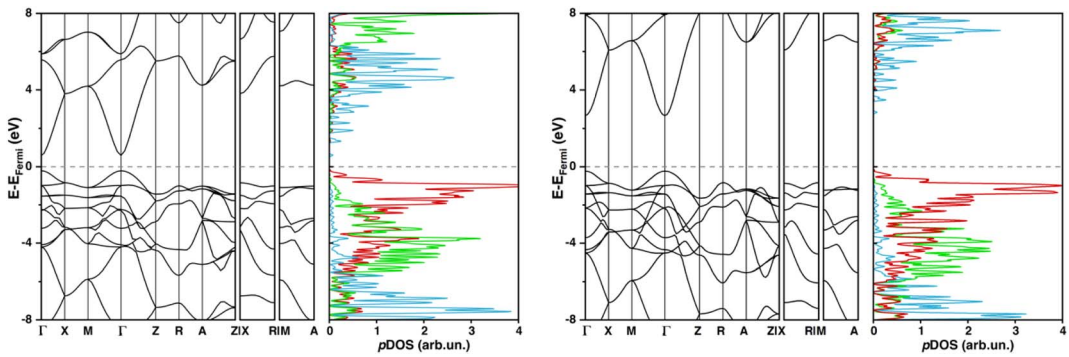

Fig. 1 Band structures and pDOS plots at PBE-D3BJ (left) and HSE06-D3BJ (right) levels of SnO_2 bulk; the color legend is Sn (s) – blue, Sn (p) – green, O (p) – red; Sn states are multiplied by 4 to better visualize CB contribution; the dashed line denotes the Fermi level.

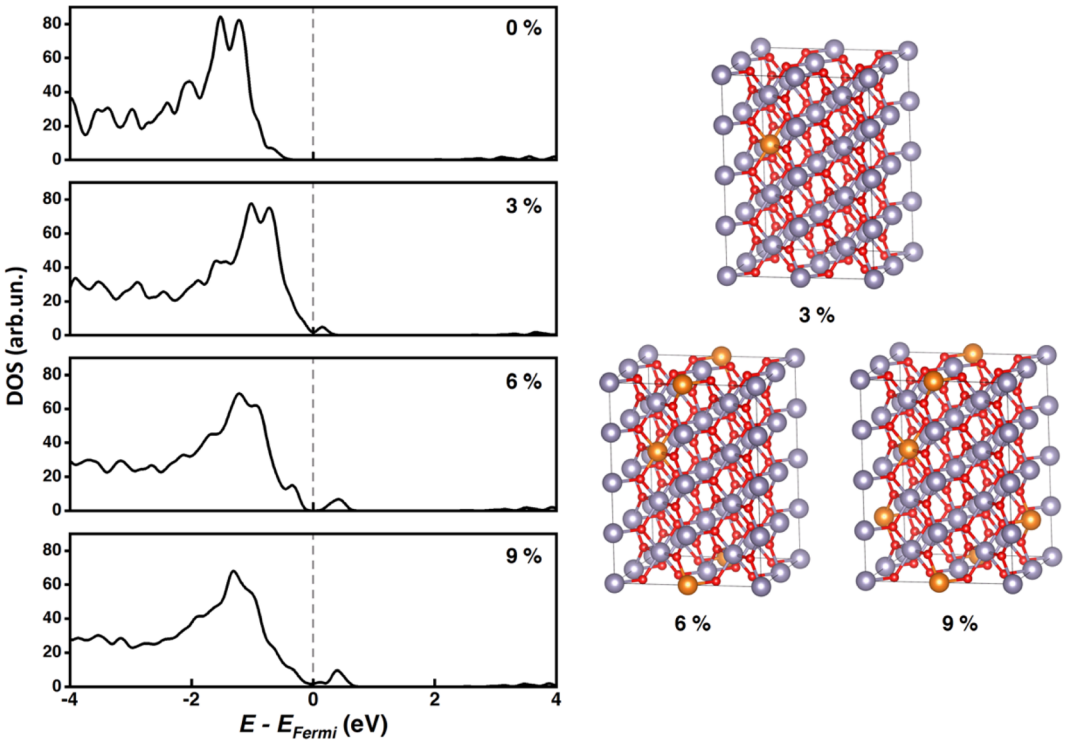

Fig. 2 On the left, total DOS calculated at the HSE06-D3BJ level for SnO_2 pristine and Mg-doped at 3, 6 and 9% where the sum over α and β spin channels is shown; the dashed line denotes the Fermi level. On the right, supercell bulk models for Mg-doped SnO_2 at 3, 6 and 9%; legend: oxygen (red), tin (grey), magnesium (orange).

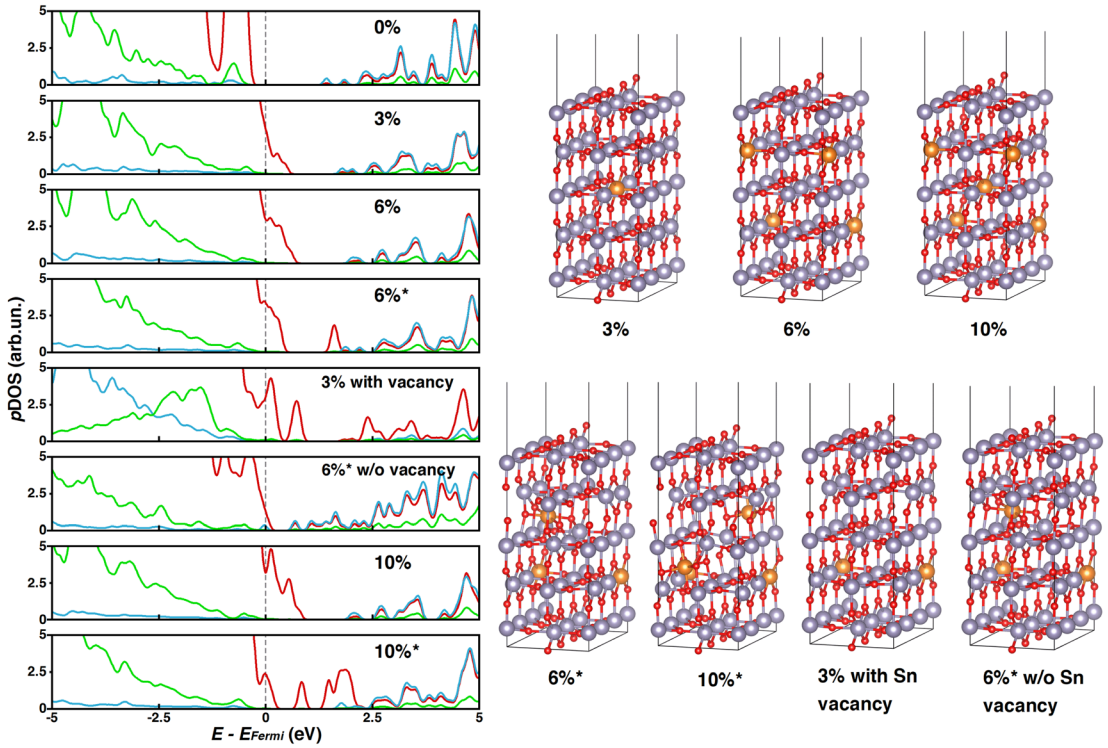

Fig. 3 pDOS calculated at the HSE06-D3BJ level for SnO_2 slab pristine and Mg-doped at 3, 6 and 10% and the related optimized slab models; the color legend is Sn (s) – blue, Sn (p) – green, O (p) – red; the dashed line denotes the Fermi level and * indicates the configuration with interstitial Mg; in particular, 6%* and 10%* contain 1 and 2 interstitial Mg, respectively.

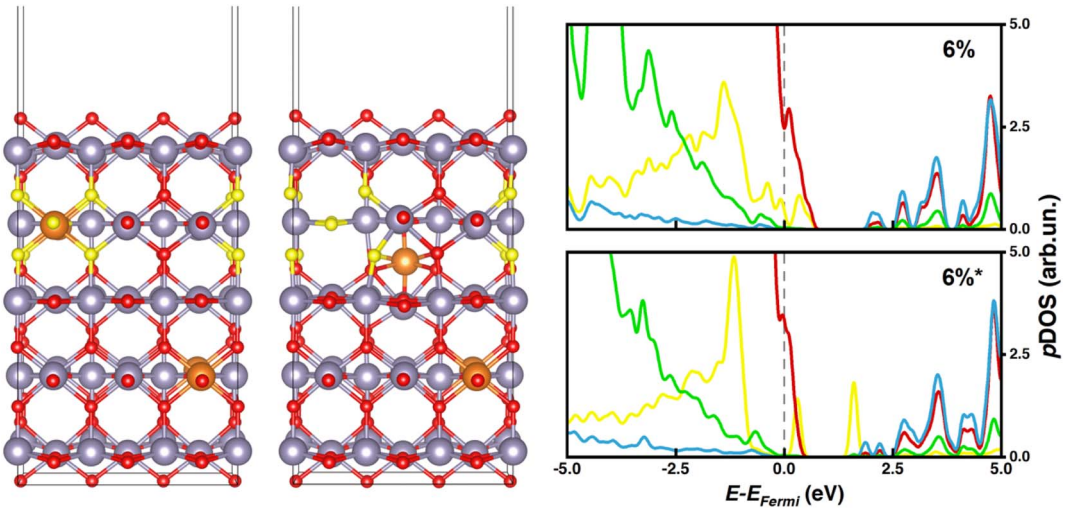

Fig. 4 6% and 6%* doped slab models with oxygen atoms mainly responsible for generating intra-gap states colored in yellow; pDOS legend: O (p) – red or yellow, Sn (s) – blue, Sn (p) – green.

corresponding to interstitial Mg-doping featured intra-gap states that could promote undesired charge recombination processes and compromise the PCE of the PSC. Our calculations reveal that such intra-gap states can be ascribed mainly to oxygen atoms neighboring tin vacancies (Fig. 4 and 5), which are significantly displaced from their atomic positions in the pristine material. To determine whether such intragap states arise from the Sn vacancy or from the interstitial Mg itself, we have considered a substitutional 3% Mg-doped slab with one Sn vacancy ($3\%_{vac}$) and a 6%* system without Sn vacancy ($6\%^*_{w/ovac}$). Computed pDOS of $3\%_{vac}$ (Fig. 3) revealed the presence of intra-gap 2p O states in line with those of 6%* and 10%* slabs, where a Sn vacancy is present. On the other hand, pDOS of $6\%^*_{w/ovac}$ (Fig. 3) presented a smaller bandgap than the corresponding 6%* slab, but does not feature oxygen intra-gap states. These decoupled results confirmed that Sn vacancies play an active role in intra-gap state generation, due to the high structural distortion of neighboring oxygen atoms, while interstitial Mg decreased the bandgap but does not generate such states. Anyhow, both effects would jeopardize PSC performances, so, from this electronic point of view, our calculations predict that Mg may be beneficial only when it occupies regular Sn lattice sites.

Doping also brings structural changes to the SnO_2 lattice. We have analyzed such distortions in terms of Pair Distribution Functions (PDFs) of Sn–O bond lengths for all doping degrees and types discussed above (Fig. 6). Besides the expected larger peak widths, substitutionally doped slabs present slightly shorter Sn–O distances than pristine material ones (in the range 1.95–2.15 Å *vs.* 2.00–2.17 Å in pure SnO_2), but neither the shape nor the range of the PDF has been affected by increasing Mg content PDF (3%)–PDF (6%)–PDF (10%). We found similar PDF

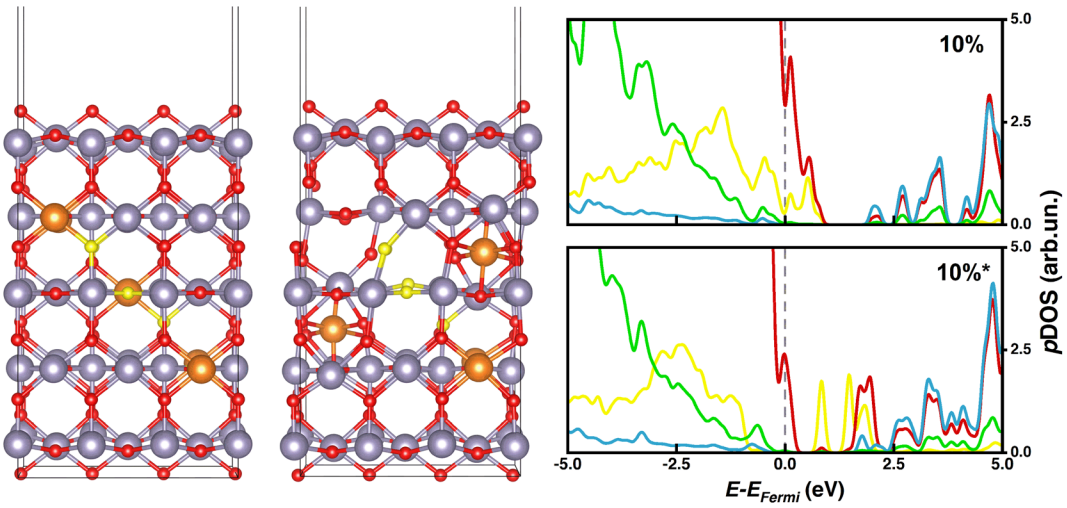

Fig. 5 10% and 10%* doped slab models with oxygen atoms mainly responsible for generating intra-gap states colored in yellow; pDOS legend: O (p) – red or yellow, Sn (s) – blue, Sn (p) – green.

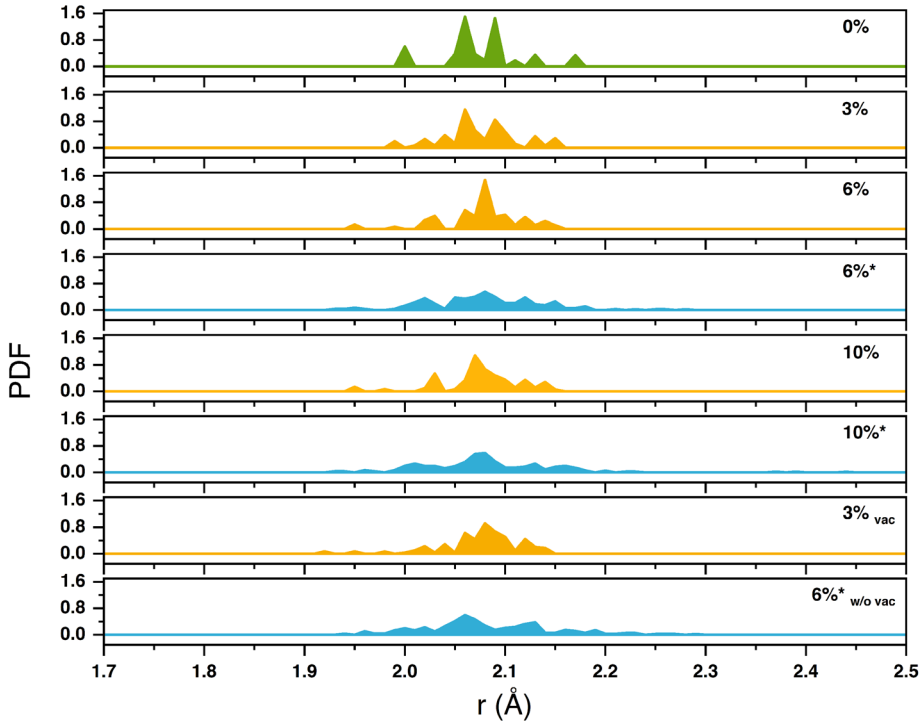

Fig. 6 Pair distribution function analysis of Sn–O distances computed for pristine and Mg-doped slabs; * indicates the configuration with interstitial Mg.

features for the other explored systems with Sn vacancies, *e.g.*, $3\%_{vac}$. This confirmed the negligible structural effects evinced experimentally between SnO_2 and Mg-doped SnO_2 with moderate Mg content, where Mg occupies only Sn sites. All systems with interstitial Mg (6%*, 10%*, and $6\%^*_{w/ovac}$) have broader PDFs ranging from 1.92 Å to 2.3 Å; Mg in interstitial sites also induces Sn–O bond elongations and overall larger distortions than substitutional Mg.

In a PSC the relative position of the CBM of the ETL and the VBM of the HTL plays a primary role in defining the V_{OC} of the entire device. Lower ETL CBM potentials lead to lower V_{OC} values.[69,70] The trend of the WF is thus connected with the VBM potential and, in the approximation of the rigid band model, also with the CBM of the material. Therefore, we can assess the change in the CBM position from the shifts of the examined WFs of the SnO_2 with different Mg doping concentrations and configurations. Briefly, lower WF values result in higher CBM potentials and, consequentially, higher V_{OC} values.

For such a reason, we have computed work function values of doped materials from HSE06-D3BJ slab calculations and resulting ΔCBM values have been plotted with respect to pristine SnO_2 in Fig. 7, and compared with experimental variations of V_{OC} at different doping levels.[35] Substitution of Mg ions in regular Sn sites produced an evident rise in CBM: higher the doping concentration, higher the CBM (Fig. 7, black dots). Interstitial Mg, instead, generates the opposite effect by lowering the CBM (Fig. 7, black stars). For this reason, the CBM of the 6% and 6*% configurations are higher/lower than that of 3% (substitutional doping). The 10*% WF value confirms this trend. These results, together with the experimental evidence of Mg occupying interstitial sites for concentrations around 8%,[23] can explain the experimental V_{OC} parameters obtained by Xiong *et al.*[35] (Fig. 7): V_{OC} increases with Mg doping reaching a maximum value at 5% and then starts to decrease.

These results confirm that moderate amounts of Mg substituting Sn in regular lattice sites enhance the performances of SnO_2 as the ETL material by pushing up the CBM and increasing the V_{OC} without creating trap states or diminishing the bandgap. In contrast, higher Mg concentrations involving

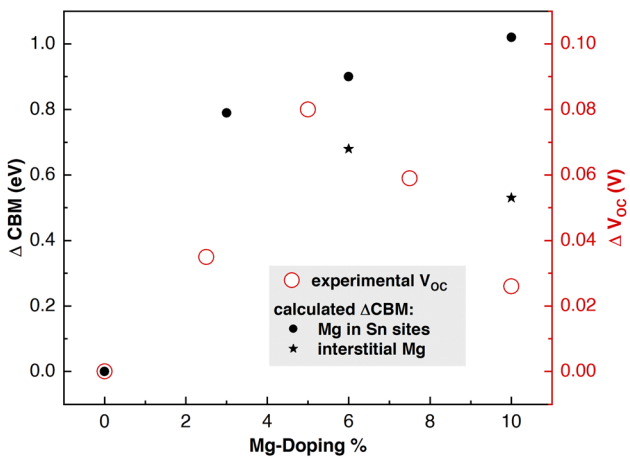

Fig. 7 Trend in $\Delta CBM = (CBM_{(x\%Mg)} - CBM_{(0\%Mg)}) = -\Delta WF$ as extracted from HSE06-D3BJ calculations at different Mg-doping percentages and the corresponding experimental ΔV_{OC}.[35]

interstitial doping have a negative impact on such performances since the V_{OC} decreases and internal structural distortions bring about undesired intra-gap states and band gap reduction.

Conclusions

In this work, we provided an atomistic characterization of Mg-ion doping effects on SnO_2 structural, electronic, and work function features, aiming at uncovering the reasons behind the PCE improvement of PSC devices incorporating doped Mg:SnO_2, which is not retained for higher-to-moderate doping degrees. Experimentally, it is found that low Mg doping of SnO_2 as the ETL slightly improves the V_{OC} of the PSC device. We ascribe this experimental evidence to electronic reasons. In particular, based on our computed work functions, we predict higher CBM for doped slabs and, consequently, an increase in V_{OC}. However, Mg^{2+} ions start to occupy interstitial sites increasing the doping concentration so the CBM goes down and thus reduces the V_{OC}. Furthermore, our analysis correlates higher structural distortions associated with interstitial Mg with bandgap reduction (due to interstitial Mg itself) and intra-gap states (due to Sn vacancies associated with interstitial Mg). Both effects could be responsible for undesired recombination processes in the PSC device and, hence, may further explain the drop in performances at high Mg doping concentrations. In conclusion, our work highlights the importance of doping effects on the electronic structure of ETL materials used in PSCs. Intra-gap states and band shifts are crucial features to be taken into account for boosting the PSC performances. We prove that intra-gap states can be fine-tuned with a proper evaluation from an atomistic/electronic structure perspective. Future investigations, exploring other dopants and ETL materials, will follow the main findings of this work to predict and design *a priori* the best dopant/ETL combination to maximize the features of PSC performance such as the V_{OC}.

Conflicts of interest

The authors declare there are no conflicts of interests.

Acknowledgements

This work was supported by the Italian Ministry of Economic Development in the framework of the Operating Agreement with ENEA for Research on the Electric System. "The computing resources and the related technical support used for this work have been provided by the CRESCO/ENEAGRID High-Performance Computing infrastructure and its staff [F. Iannone *et al.*]. The CRESCO/ENEAGRID High-Performance Computing infrastructure is funded by ENEA, the Italian National Agency for New Technologies, Energy and Sustainable Economic Development and by Italian and European research programs (see **https://www.cresco.enea.it/englishforinformation**)". The authors also wish to thank the National Research Foundation, Prime Minister's Office, Singapore under the Solar CRP (S18-1176-SCRP) for financial support.

References

1 Q. Jiang, Z. Chu, P. Wang, X. Yang, H. Liu, Y. Wang, Z. Yin, J. Wu, X. Zhang and J. You, Planar-Structure Perovskite Solar Cells with Efficiency beyond 21%, *Adv. Mater.*, 2017, **29**, 1703852.
2 A. B. Muñoz-García, I. Benesperi, G. Boschloo, J. J. Concepcion, J. H. Delcamp, E. A. Gibson, G. J. Meyer, M. Pavone, H. Pettersson, A. Hagfeldt and M. Freitag, Dye-sensitized solar cells strike back, *Chem. Soc. Rev.*, 2021, **50**, 12450–12550.
3 F. Schipani, D. R. Miller, M. A. Ponce, C. M. Aldao, S. A. Akbar, P. A. Morris and J. C. Xu, Conduction mechanisms in SnO2 single-nanowire gas sensors: An impedance spectroscopy study, *Sens. Actuators, B*, 2017, **241**, 99–108.
4 V. B. Raj, A. T. Nimal, M. Tomar, M. U. Sharma and V. Gupta, Novel scheme to improve SnO2/SAW sensor performance for NO2 gas by detuning the sensor oscillator frequency, *Sens. Actuators, B*, 2015, **220**, 154–161.
5 H. Kim and A. Piqué, Transparent conducting Sb-doped SnO2 thin films grown by pulsed-laser deposition, *Appl. Phys. Lett.*, 2004, **84**, 218–220.
6 Y. Idota, T. Kubota, A. Matsufuji, Y. Maekawa and T. Miyasaka, Tin-Based Amorphous Oxide: A High-Capacity Lithium-Ion-Storage Material, *Science*, 1997, **276**, 1395–1397.
7 K. G. Godinho, A. Walsh and G. W. Watson, Energetic and Electronic Structure Analysis of Intrinsic Defects in SnO2, *J. Phys. Chem. C*, 2009, **113**, 439–448.
8 Ç. Kılıç and A. Zunger, Origins of Coexistence of Conductivity and Transparency in SnO_2, *Phys. Rev. Lett.*, 2002, **88**, 095501.
9 L. Xiong, Y. Guo, J. Wen, H. Liu, G. Yang, P. Qin and G. Fang, Review on the Application of SnO2 in Perovskite Solar Cells, *Adv. Funct. Mater.*, 2018, **28**, 1802757.
10 H. Kim, R. C. Y. Auyeung and A. Piqué, Transparent conducting F-doped SnO2 thin films grown by pulsed laser deposition, *Thin Solid Films*, 2008, **516**, 5052–5056.
11 J. Ouerfelli, S. O. Djobo, J. C. Bernède, L. Cattin, M. Morsli and Y. Berredjem, Organic light emitting diodes using fluorine doped tin oxide thin films, deposited by chemical spray pyrolysis, as anode, *Mater. Chem. Phys.*, 2008, **112**, 198–201.
12 H. Toyosaki, M. Kawasaki and Y. Tokura, Electrical properties of Ta-doped SnO2 thin films epitaxially grown on TiO2 substrate, *Appl. Phys. Lett.*, 2008, **93**, 132109.
13 K. Jain, R. P. Pant and S. T. Lakshmikumar, Effect of Ni doping on thick film SnO2 gas sensor, *Sens. Actuators, B*, 2006, **113**, 823–829.
14 J. Kaur, R. Kumar and M. C. Bhatnagar, Effect of indium-doped SnO2 nanoparticles on NO2 gas sensing properties, *Sens. Actuators, B*, 2007, **126**, 478–484.
15 Z. Lin, N. Li, Z. Chen and P. Fu, The effect of Ni doping concentration on the gas sensing properties of Ni doped SnO2, *Sens. Actuators, B*, 2017, **239**, 501–510.

16 S. Akin, Hysteresis-Free Planar Perovskite Solar Cells with a Breakthrough Efficiency of 22% and Superior Operational Stability over 2000 h, *ACS Appl. Mater. Interfaces*, 2019, **11**, 39998–40005.

17 E. Halvani Anaraki, A. Kermanpur, M. T. Mayer, L. Steier, T. Ahmed, S.-H. Turren-Cruz, J. Seo, J. Luo, S. M. Zakeeruddin, W. R. Tress, T. Edvinsson, M. Grätzel, A. Hagfeldt and J.-P. Correa-Baena, Low-Temperature Nb-Doped SnO2 Electron-Selective Contact Yields over 20% Efficiency in Planar Perovskite Solar Cells, *ACS Energy Lett.*, 2018, **3**, 773–778.

18 H. Ye, Z. Liu, X. Liu, B. Sun, X. Tan, Y. Tu, T. Shi, Z. Tang and G. Liao, 17.78% efficient low-temperature carbon-based planar perovskite solar cells using Zn-doped SnO2 electron transport layer, *Appl. Surf. Sci.*, 2019, **478**, 417–425.

19 G. V. Sannino, A. De Maria, V. La Ferrara, G. Rametta, L. V. Mercaldo, M. L. Addonizio, L. Lancellotti, A. Pecoraro, A. B. Muñoz-García, M. Pavone and P. Delli Veneri, Development of SnO_2 Composites as Electron Transport Layer in Unencapsulated CH3NH3PbI3 Solar Cells, *Solids*, 2021, **2**, 407–419.

20 L. Chouhan, S. K. Panda, S. Bhattacharjee, B. Das, A. Mondal, B. N. Parida, R. Brahma, M. K. Manglam, M. Kar, G. Bouzerar and S. K. Srivastava, Room temperature d0 ferromagnetism, zero dielectric loss and ac-conductivity enhancement in p-type Ag-doped SnO2 compounds, *J. Alloys Compd.*, 2021, **870**, 159515.

21 S. K. Srivastava, P. Lejay, B. Barbara, S. Pailhès, V. Madigou and G. Bouzerar, Possible room-temperature ferromagnetism in K-doped SnO2: X-ray diffraction and high-resolution transmission electron microscopy study, *Phys. Rev. B: Condens. Matter Mater. Phys.*, 2010, **82**, 193203.

22 W. Wei, Y. Dai, M. Guo, K. Lai and B. Huang, Density functional study of magnetic properties in Zn-doped SnO2, *J. Appl. Phys.*, 2010, **108**, 093901.

23 P. Wu, B. Zhou and W. Zhou, Room-temperature ferromagnetism in epitaxial Mg-doped SnO2 thin films, *Appl. Phys. Lett.*, 2012, **100**, 182405.

24 W.-Z. Xiao, L.-L. Wang and Z. Tan, Unexpected magnetic properties in carbon-doped SnO2 from first-principles calculation, *Comput. Mater. Sci.*, 2014, **83**, 5–11.

25 D. O. Scanlon and G. W. Watson, On the possibility of p-type SnO2, *J. Mater. Chem.*, 2012, **22**, 25236–25245.

26 C. E. Benouis, M. Benhaliliba, F. Yakuphanoglu, A. T. Silver, M. S. Aida and A. S. Juarez, Physical properties of ultrasonic sprayed nanosized indium doped SnO2 films, *Synth. Met.*, 2011, **161**, 1509–1516.

27 Z. Ji, Z. He, Y. Song, K. Liu and Z. Ye, Fabrication and characterization of indium-doped p-type SnO2 thin films, *J. Cryst. Growth*, 2003, **259**, 282–285.

28 T. Le, H. P. Dang and V. H. Le, Determination of the optimum annealing temperature and time for Indium-doped SnO2 films to achieve the best p-type conductive property, *J. Alloys Compd.*, 2017, **696**, 1314–1322.

29 W. Ben Haj Othmen, Z. Ben Hamed, B. Sieber, A. Addad, H. Elhouichet and R. Boukherroub, Structural and optical characterization of p-type highly Fe-doped SnO2 thin films and tunneling transport on SnO2:Fe/p-Si heterojunction, *Appl. Surf. Sci.*, 2018, **434**, 879–890.

30 X. Li, R. Deng, Y. Li, B. Yao, Z. Ding, J. Qin and Q. Liang, Effect of Mg doping on optical and electrical properties of SnO2 thin films: An experiment and first-principles study, *Ceram. Int.*, 2016, **42**, 5299–5303.

31 H. He, Z. Xie, Q. Li, J. Li and Q. Zhang, Novel p-type conductivity in SnO2 thin films by Mg doping, *J. Alloys Compd.*, 2017, **714**, 258–262.

32 H. He, Z. Xie, Q. Li and H. Niu, On the possibility of p-type doping of SnO2 with Mg: A first-principles study, *Comput. Mater. Sci.*, 2015, **101**, 62–65.

33 W. Fu, M. Li, J. Li, G. Fang, P. Ye, E. Wentao, X. Xiao, H. Wei, B. Liu, Y. Lu and Y. He, Achieving p-type conductivity in wide-bandgap SnO2 by a two-step process, *Appl. Phys. Lett.*, 2021, **118**, 112102.

34 B. Chakraborty and L. M. Ramaniah, Exploring d0 magnetism in doped SnO2–a first principles DFT study, *J. Magn. Magn. Mater.*, 2015, **385**, 207–216.

35 L. Xiong, M. Qin, G. Yang, Y. Guo, H. Lei, Q. Liu, W. Ke, H. Tao, P. Qin, S. Li, H. Yu and G. Fang, Performance enhancement of high temperature SnO2-based planar perovskite solar cells: electrical characterization and understanding of the mechanism, *J. Mater. Chem. A*, 2016, **4**, 8374–8383.

36 N. Zhou, Q. Cheng, L. Li and H. Zhou, Doping effects in SnO2 transport material for high performance planar perovskite solar cells, *J. Phys. D: Appl. Phys.*, 2018, **51**, 394001.

37 G. Kresse and J. Furthmüller, Efficient iterative schemes for ab initio total-energy calculations using a plane-wave basis set, *Phys. Rev. B: Condens. Matter Mater. Phys.*, 1996, **54**, 11169–11186.

38 G. Kresse and J. Furthmüller, Efficiency of ab-initio total energy calculations for metals and semiconductors using a plane-wave basis set, *Comput. Mater. Sci.*, 1996, **6**, 15–50.

39 G. Kresse and J. Hafner, Ab initio molecular dynamics for liquid metals, *Phys. Rev. B: Condens. Matter Mater. Phys.*, 1993, **47**, 558–561.

40 G. Kresse and J. Hafner, Ab initio molecular-dynamics simulation of the liquid-metal-amorphous-semiconductor transition in germanium, *Phys. Rev. B: Condens. Matter Mater. Phys.*, 1994, **49**, 14251–14269.

41 J. P. Perdew, K. Burke and M. Ernzerhof, Generalized Gradient Approximation Made Simple, *Phys. Rev. Lett.*, 1996, **77**, 3865–3868.

42 J. P. Perdew, K. Burke and M. Ernzerhof, Generalized Gradient Approximation Made Simple, *Phys. Rev. Lett.*, 1996, **77**, 3865; *Phys. Rev. Lett.*, 1997, **78**, 1396.

43 J. Heyd, G. E. Scuseria and M. Ernzerhof, Hybrid functionals based on a screened Coulomb potential, *J. Chem. Phys.*, 2003, **118**, 8207–8215.

44 J. Heyd, G. E. Scuseria and M. Ernzerhof, Erratum: "Hybrid functionals based on a screened Coulomb potential", *J. Chem. Phys.*, 2003, **118**, 8207; *J. Chem. Phys.*, 2006, **124**, 219906.

45 P. E. Blöchl, Projector augmented-wave method, *Phys. Rev. B: Condens. Matter Mater. Phys.*, 1994, **50**, 17953–17979.

46 G. Kresse and D. Joubert, From ultrasoft pseudopotentials to the projector augmented-wave method, *Phys. Rev. B: Condens. Matter Mater. Phys.*, 1999, **59**, 1758–1775.
47 S. Grimme, S. Ehrlich and L. Goerigk, Effect of the damping function in dispersion corrected density functional theory, *J. Comput. Chem.*, 2011, **32**, 1456–1465.
48 A. D. Becke and E. R. Johnson, A density-functional model of the dispersion interaction, *J. Chem. Phys.*, 2005, **123**, 154101.
49 C. Baiano, E. Schiavo, C. Gerbaldi, F. Bella, G. Meligrana, G. Talarico, P. Maddalena, M. Pavone and A. B. Muñoz-García, Role of surface defects in CO2 adsorption and activation on CuFeO2 delafossite oxide, *Mol. Catal.*, 2020, **496**, 111181.
50 M. D'Arienzo, L. Gamba, F. Morazzoni, U. Cosentino, C. Greco, M. Lasagni, D. Pitea, G. Moro, C. Cepek, V. Butera, E. Sicilia, N. Russo, A. B. Muñoz-García and M. Pavone, Experimental and Theoretical Investigation on the Catalytic Generation of Environmentally Persistent Free Radicals from Benzene, *J. Phys. Chem. C*, 2017, **121**, 9381–9393.
51 A. B. Muñoz-García and M. Pavone, Structure and energy level alignment at the dye–electrode interface in p-type DSSCs: new hints on the role of anchoring modes from ab initio calculations, *Phys. Chem. Chem. Phys.*, 2015, **17**, 12238–12246.
52 A. B. Muñoz-García, F. Sannino, G. Vitiello, D. Pirozzi, L. Minieri, A. Aronne, P. Pernice, M. Pavone and G. D'Errico, Origin and Electronic Features of Reactive Oxygen Species at Hybrid Zirconia-Acetylacetonate Interfaces, *ACS Appl. Mater. Interfaces*, 2015, **7**, 21662–21667.
53 B. Samanta, Á. Morales-García, F. Illas, N. Goga, J. A. Anta, S. Calero, A. Bieberle-Hütter, F. Libisch, A. B. Muñoz-García, M. Pavone and M. Caspary Toroker, Challenges of modeling nanostructured materials for photocatalytic water splitting, *Chem. Soc. Rev.*, 2022, **51**, 3794–3818.
54 A. A. Bolzan, C. Fong, B. J. Kennedy and C. J. Howard, Structural Studies of Rutile-Type Metal Dioxides, *Acta Crystallogr., Sect. B: Struct. Sci.*, 1997, **53**, 373–380.
55 R. Shannon, Revised effective ionic radii and systematic studies of interatomic distances in halides and chalcogenides, *Acta Crystallogr., Sect. A: Cryst. Phys., Diffr., Theor. Gen. Crystallogr.*, 1976, **32**, 751–767.
56 J. Oviedo and M. J. Gillan, Energetics and structure of stoichiometric SnO2 surfaces studied by first-principles calculations, *Surf. Sci.*, 2000, **463**, 93–101.
57 Y. Duan, Electronic properties and stabilities of bulk and low-index surfaces of SnO in comparison with SnO2: A first-principles density functional approach with an empirical correction of van der Waals interactions, *Phys. Rev. B: Condens. Matter Mater. Phys.*, 2008, **77**, 045332.
58 A. Pecoraro, A. De Maria, P. Delli Veneri, M. Pavone and A. B. Muñoz-García, Interfacial electronic features in methyl-ammonium lead iodide and p-type oxide heterostructures: new insights for inverted perovskite solar cells, *Phys. Chem. Chem. Phys.*, 2020, **22**, 28401–28413.
59 G. Zhang, G. Qin, G. Yu, Q. Hu, H. Fu and C. Shao, Ab initio investigation on a promising transparent conductive oxide, Nb:SnO2, *Thin Solid Films*, 2012, **520**, 5965–5970.
60 D. Fröhlich, R. Kenklies and R. Helbig, Band-Gap Assignment in SnO_2 by Two-Photon Spectroscopy, *Phys. Rev. Lett.*, 1978, **41**, 1750–1751.
61 P. D. Borges, L. M. R. Scolfaro, H. W. Leite Alves and E. F. da Silva, DFT study of the electronic, vibrational, and optical properties of SnO2, *Theor. Chem. Acc.*, 2010, **126**, 39–44.
62 X. Cai, P. Zhang and S.-H. Wei, Revisit of the band gaps of rutile SnO2 and TiO2: a first-principles study, *J. Semicond.*, 2019, **40**, 092101.
63 A. Stashans, P. Puchaicela and R. Rivera, DFT study of chromium-doped SnO2 materials, *J. Mater. Sci.*, 2014, **49**, 2904–2911.
64 M. Worsdale, A. Rabis, E. Fabbri, T. J. Schmidt and D. Kramer, Conductivity Limits of Extrinsically Doped SnO2 Supports, *ECS Trans.*, 2015, **69**, 1167–1178.
65 J. Xue, S. Ma, Q. Bi, X. Zhang, W. Guan and Y. Gao, Revealing the modification mechanism of La-doped Ti/SnO2 electrodes related to the microelectronic structure by first-principles calculations, *J. Alloys Compd.*, 2018, **747**, 423–430.
66 W. A. Farooq, S. M. Ali, J. Muhammad, S. D. Ali, M. H. Aziz, N.-u. Rehman and M. Hussain, Synthesis and characterization of Sn1Mg1−xO2 thin films fabricated by aero-sole assisted chemical vapor deposition, *J. Mater. Sci.: Mater. Electron.*, 2013, **24**, 5140–5146.
67 N. Mazumder, A. Bharati, S. Saha, D. Sen and K. K. Chattopadhyay, Effect of Mg doping on the electrical properties of SnO2 nanoparticles, *Curr. Appl. Phys.*, 2012, **12**, 975–982.
68 B. Thomas and B. Skariah, Spray deposited Mg-doped SnO2 thin film LPG sensor: XPS and EDX analysis in relation to deposition temperature and doping, *J. Alloys Compd.*, 2015, **625**, 231–240.
69 K. Mahmood, S. Sarwar and M. T. Mehran, Current status of electron transport layers in perovskite solar cells: materials and properties, *RSC Adv.*, 2017, **7**, 17044–17062.
70 B. A. Gregg and M. C. Hanna, Comparing organic to inorganic photovoltaic cells: Theory, experiment, and simulation, *J. Appl. Phys.*, 2003, **93**, 3605–3614.